Journal of Polymers and the Environment (2024) 32:4315–4329
https://doi.org/10.1007/s10924-024-03232-6

ORIGINAL PAPER

Efficiently Recyclable Fe-Doped ZnO/Bacterial Cellulose-Based Composite Aerogel for Photocatalytic Degradation of Methylene Blue Under Visible Light

Xutao Zhang[1] · Weiliang Chen[1] · Xiangqi Li[1]

Accepted: 18 February 2024 / Published online: 26 March 2024

Abstract
Excellent photocatalytic performance and recyclability are crucial for the long-term use of the photocatalyst. In this study, 5 mol% Fe doped zinc oxide (ZF5), was freeze-dried with bacterial cellulose (BC)/sodium alginate (SA) solution to fabricate a novel composite aerogel capable of degrading methylene blue (MB) under visible light. Ca^{2+} crosslinking and hydrophobic modifications were adopted to strengthen the aerogel skeleton and enhance the cycling photocatalytic activity, meanwhile, making the aerogel floatable persistently. The influences of pH, ZF5 dosage, and initial solution concentration on MB degradation were investigated. Benefiting from the synergy between the components and the combined modification, the optimum composite aerogel exhibits photocatalytic efficiency of up to 97.4% at an initial MB concentration of 20 mg/L within an irradiation time of 80 min. In addition, it exhibits a degradation efficiency of 79.7% even after 8 cycles, showing great potential in visible-light-driven degradation of MB.

Keywords Fe-doped ZnO · Bacteria cellulose-based composite aerogel · Photocatalysis · Methylene blue · Hydrophobic modification

Introduction

Over the past few years, there has been a significant increase in the use of synthetic dyes in industries such as textiles, paints, leather, and others, resulting in the discharge of numerous untreated dye residues into environmental water bodies. These dye pollutants are typically resistant to decomposition and possess toxic and carcinogenic properties. Moreover, their transmission through the food chain significantly jeopardizes human health [1–5]. Therefore, developing a long-term, efficient, and sustainable approach for treating dye wastewater is imperative. Various methods, such as biotechnology, chemical reactions, and physical treatments, have been employed to address this issue [6, 7]. Notably, in recent years, there has been a growing focus on the photocatalytic degradation technology due to its exceptional efficiency, cost-effectiveness, and absence of pollution residues post-degradation.

ZnO, being a promising third-generation semiconductor material, is frequently selected as an excellent photocatalyst for the degradation of dye pollution due to its exceptional performance resulting from its strong UV absorption from the solar spectrum [8]. Nevertheless, ZnO possesses certain drawbacks, including the tendency for recombination of electron-hole pairs, a wide band gap, and a limited ability to collect visible light, all of which considerably impede the overall photocatalytic efficiency [9]. Currently, the metal cation doping strategy has been proposed for ZnO to broaden its light absorption range and enhance its catalytic performance under sunlight [10, 11]. Fe^{3+} ions doped in ZnO lattice, can act as shallow electron traps and effectively mitigate electron-hole recombination, resulting in enhanced photocatalytic activity [12]. Furthermore, Fe^{3+}-doped ZnO shows an improved visible light response compared to pure ZnO and is proven to be a promising visible-light-driven photocatalyst [13]. On the other hand, semiconductor nanomaterial is preferred to be considered in photocatalytic applications because of its high surface area. However, the nanoparticles tend to agglomerate and settle at the bottom, making recycling challenging and negatively

✉ Xiangqi Li
lxiangqi@fzu.edu.cn

[1] College of Materials Science and Engineering, Fuzhou University, Fuzhou 350108, China

impacting their photocatalytic performance [14]. To address this issue, incorporating photocatalyst particles into a suitable matrix has been explored to improve the reusability, stability, and activity of photocatalysts [15, 16]. Using porous expanded perlite (EP) as a carrier, Hai et al. [17] prepared a floating mpg-C_3N_4/EP photocatalyst, and found it showed superior photocatalytic activity over mpg-C_3N_4 powder in the case of unstirring. However, this study did not assess the persistence of floatability, which is crucial to the cycling performance of photocatalysts.

Bacterial cellulose (BC) aerogel, usually formed by freeze-drying BC aqueous solution, is an amphiphilic ultra-light material with high porosity (up to 99%). It has been extensively researched as an adsorbent and carrier for water remediation, owing to its high porosity, abundant surface hydroxyl groups, and environmental friendliness [18–22]. To improve its mechanical and chemical properties, BC normally needs to be modified and functionalized via grafting functional groups or integrating inorganic nanomaterial. Pereira et al. [23] developed functionalized BC aerogels via oxidation and silanization and found the functionalized aerogels had better mechanical and absorptive properties for water/oil separation and organic solvent adsorption. Using glutaraldehyde as a cross-linking agent, Jiang et al. [24] prepared Ag_2O-loaded BC aerogel containing zwitterionic compounds by freeze-drying and step-by-step immersing method. The obtained Ag_2O-loaded BC aerogel showed high photodegradation efficiency to MB and good stability, but the preparation process involving two freeze-drying and two dipping steps was time-consuming. In this study, MB is adopted as a simulated organic pollutant due to its toxicity and carcinogenicity character, and a simple and time-saving method is proposed to prepare a novel BC-based composite aerogel capable of degrading MB. The mixture of Fe-doped ZnO nanoparticles, SA, and BC solutions was one-step freeze-dried and subsequently modified by spraying an alcoholic solution of $CaCl_2$ and chemical vapor deposition of methyltrimethoxysilane. The BC/SA aerogel not only acts as a structural support for the dispersed Fe-doped ZnO photocatalyst but also provides a large number of active sites for the adsorption of pollutants because its rich surface hydroxyl groups can facilitate the formation of hydrogen bonding and electrostatic interactions. In addition, the combined modification can strengthen the aerogel skeleton and make the aerogel floatable persistently. The obtained composite aerogel exhibits excellent visible-light-driven degradation performance and recyclability.

Experimental

Materials

The chemicals used in this study were sourced from reputable suppliers. Zinc diacetate dihydrate ($Zn(CH_3COO)_2{\cdot}2H_2O$), ferric chloride hexahydrate ($FeCl_3{\cdot}6H_2O$), sodium hydroxide (NaOH), hydrochloric acid (HCl, 99.8%), ammonia (NH_4OH) and anhydrous calcium chloride ($CaCl_2$) were obtained from Sinopharm Chemical Reagent (Shanghai, China). Sodium alginate (SA), methyltrimethoxysilane (MTMS), disodium ethylenediaminetetraacetic acid (EDTA-2Na), p-benzoquinone (BQ) and isopropyl alcohol (IPA) were procured from Shanghai Aladdin Biochemical Technology Co., Ltd, and bacterial cellulose (BC) hydrogel with a concentration of 0.8 wt% was supplied by Guangxi Qihong Reagent. Deionized water was utilized throughout the experimental procedures.

Synthesis of Fe-Doped ZnO

Fixing the total number of moles of Fe^{3+} and Zn^{2+} ions at 0.0456 mol, $FeCl_3{\cdot}6H_2O$ and $Zn(CH_3COO)_2{\cdot}2H_2O$ were dissolved in 85 mL of deionized water and stirred for 1 h to achieve a homogeneous solution. Subsequently, 15 mL of 4.67 M NaOH solution was slowly added to the mixed solution with continuous stirring for 2 h, and a yellow product was obtained. After washing with deionized water and absolute ethanol three times, the obtained precipitate was dried at 80 °C for 24 h, followed by calcination at 500 °C for 2 h. Finally, Fe-doped ZnO with Fe^{3+} content of 0, 1 mol%, 3 mol%, 5 mol%, and 10 mol% were obtained, and labeled as Z, ZF1, ZF3, ZF5, and ZF10, respectively.

Preparation and Modification of ZF5-BS Composite Aerogel

Figure 1 depicts the preparation and modification processes of ZF5/BC/SA (ZF5-BS) composite aerogel. First, 5 g of 0.8 wt% BC hydrogel and a certain mass of ZF5 (0.1, 0.2, 0.3, and 0.4 g) were magnetically stirred in a 25 mL beaker for 1 h, and then 5 g of SA aqueous solution (0.8 wt%) was added and continuously stirred for 3 h, followed by an ultrasonic vibration for 20 min. The yielded solution was pre-frozen in a freeze dryer at − 55 °C for 12 h and vacuum dried for 48 h, and then ZF5-BS composite aerogel with a cylindrical shape was obtained. A crosslinking modification was performed by spraying ZF5-BS with an alcoholic solution rather than an aqueous solution of $CaCl_2$ (1.2 wt%) to achieve crosslinking, meanwhile avoiding the drying shrinkage deformation. The cross-linked aerogel was named ZF5-BSC. A series of ZF5-BSC composite aerogels with different mass ratios of ZF5 to BS precursor (1:100, 2:100, 3:100, and 4:100), were prepared and denoted as 1ZF5-BSC, 2ZF5-BSC, 3ZF5-BSC, and 4ZF5-BSC, respectively. For comparison, Ca^{2+}-crosslinked BC/SA aerogel without ZF5 was also prepared and denoted as BSC. A hydrophobic modification

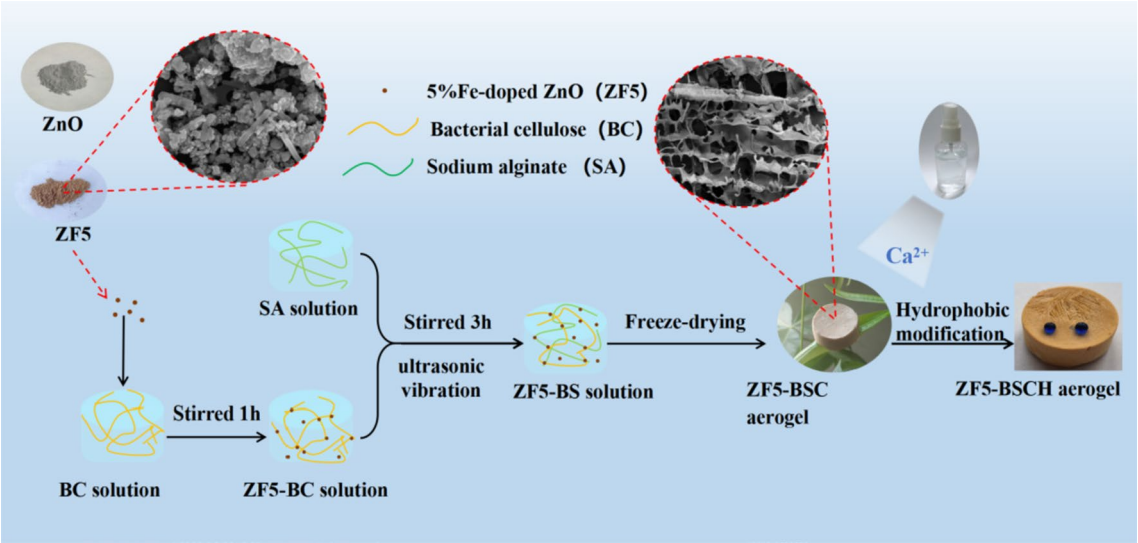

Fig. 1 Preparation of ZF5-BSCH composite aerogel

of 3ZF5-BSC was performed using 2 mL ammonia and 2 mL MTMS via chemical vapor deposition, and then 3ZF5-BSCH composite aerogel was obtained.

Characterization

The phase identification of ZnO doped with varying Fe content was conducted using a Miniflex-600 X-ray diffractometer (XRD, Nihon Rikaku Co., Japan) with Cu-Kα1 radiation (λ = 1.5406 Å) at a scanning rate of 5°/min from 20 to 80°. The microstructure of the composite aerogel was examined using a Sigma-500 field emission scanning electron microscope (SEM, Carl Zeiss, Germany). Fourier transform infrared spectrometry (FT-IR, Thermo Fisher Scientific Inc., USA) test was performed in the range of 400–4000 cm^{-1} using a Nicolet-5700 spectrometer with a resolution of 4 cm^{-1} to investigate the chemical bonds and functional groups in the different samples. The surface element chemical states were analyzed using a K-Alpha + X-ray photoelectron spectroscopy (XPS, Thermo Fisher Scientific Inc., USA) with monochromatized Al Kα1 excitation. The UV–Vis diffuse reflection absorption (UV–Vis, PerkinElmer Inc., USA) of Fe-doped ZnO was measured using a Lambda-950 spectrophotometer in the wavelength range of 250–700 nm, with $BaSO_4$ as the reference. The UV–Vis diffuse reflection absorption of MB was measured in the wavelength range of 500–750 nm. The compressive stress-strain curves of the 3ZF5-BS, 3ZF5-BSC, and 3ZF5-BSCH composite aerogels were performed on an electronic universal testing machine (MTS E43.104, Meters Industrial System Co., USA). The photoluminescence spectra (PL, HORIBA Ltd., Japan) were measured on fluorescence spectrometrywith an Xe laser excitation source (λ = 325 nm) by FluoroMax-4.

Photocatalytic Experiments

The photocatalytic degradation of MB was conducted using a 300 W xenon lamp (PLS-SXE300+) chemical reaction unit at ambient temperature, with an ultraviolet cut-off glass filter (λ > 420 nm) to ensure only visible light was used. The experimental procedure involved dispersing 100 mg of Fe-doped ZnO in a 20 mL MB solution with a concentration of 20 mg/L at ambient temperature. The suspension was stirred in the dark for 30 min to reach an adsorption-desorption equilibrium before initiating the photocatalytic degradation process. The specimens were taken every 20 min during the illumination. A similar experiment was also performed by replacing Fe-doped ZnO powder with a quarter of the cylindrical ZF5-BS composite aerogel.

The MB concentrations were calibrated using the Beer-Lambert law at λ max values of 664 nm. The photocatalytic degradation efficiency (η) of the photocatalyst to MB was calculated by the following equation [25]:

$$\eta(\%) = \frac{C_0 - C}{C_0} \times 100\% \quad (1)$$

where C_0 and C represent the initial MB concentration and the MB concentration at the sampling time t, respectively.

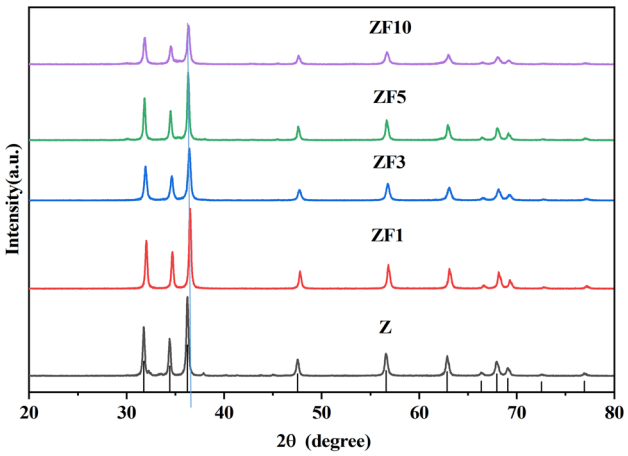

Fig. 2 XRD patterns of Fe-doped ZnO samples

Table 1 Lattice parameters (nm) and crystal cell (nm^3) volume of Fe-doped ZnO

Sample	Lattice constants		The volume of crystal cell
	a	c	
Z	0.32464	0.52000	0.04839
ZF1	0.32443	0.51944	0.04829
ZF3	0.32451	0.51908	0.04832
ZF5	0.32442	0.51994	0.04828
ZF10	0.32464	0.51954	0.04838

Results and Discussion

Characterization Results

X-ray diffraction (XRD) patterns were utilized to determine the crystal structure and phase composition of Fe-doped ZnO. As shown in Fig. 2, the XRD patterns of all samples exhibit consistency with JCPDS card No. 36-1451, confirming the presence of single-phase ZnO with a hexagonal wurtzite structure. There is no diffraction peak of Fe oxide impurity present for Fe-doped ZnO samples. Table 1 gives the lattice parameters of all the samples. All the Fe-doped ZnO samples exhibit lattice shrinkage compared to the pure ZnO sample, which may be attributed to the substitution of Fe^{3+} with a small ionic radius (0.064 nm) for Zn^{2+} (0.074 nm) in the ZnO lattice [26]. Moreover, zinc vacancies can occur along with the unequal-valent substitution between Fe^{3+} and Zn^{2+} to balance the charge, as expressed in the following reaction equation [27]:

$$Fe_2O_3 \xrightarrow{ZnO} 2Fe_{Zn}^{\cdot} + V_{Zn}'' + 3O_O \quad (2)$$

where $Fe_{Zn}^{\cdot}$ represents the substitution of Fe^{3+} for Zn^{2+} in the lattice, resulting in a positive charge, and V_{Zn}'' represents a zinc vacancy with two negative charges. The zinc vacancies can also contribute to the lattice shrinkage of Fe-doped ZnO.

The SEM was employed to investigate the morphologies of the particles and composite aerogels. As depicted in Fig. 3a, b and Z is mainly composed of spherical particles, while ZF5 particles exhibit spherical and rod shapes. It can also be observed that ZF5 shows finer and more uniform particle size relative to Z. These results indicate that the Fe^{3+} doping not only affects the shape of ZnO grain but also inhibits its growth. Figure 3c shows the 3ZF5-BSC composite aerogel has a highly porous structure with a large number of micrometer pores distributed between the cellulose sheets. From Fig. 3d–f, it can be seen that the BS aerogel exhibits quite different surface characteristics from 3ZF5-BSC and 3ZF5-BSCH aerogels. The BS aerogel has a relatively smooth surface of cellulose sheets with interwoven nanofibers, while the 3ZF5-BSC and 3ZF5-BSCH aerogels exhibit a similar rough surface embedded with ZF5 spheres and rods, and the cellulose sheets are almost covered.

FT-IR is an important tool for group identification. Figure 4a shows the spectra of BS and 3ZF5-BS aerogels before and after modification. In the spectrum of BS, the absorption of 3360 cm^{-1} comes from the stretching vibration of –OH, the characteristic absorption around 1422 cm^{-1} is assigned to the carboxyl C=O stretching vibration, and the absorption peak at 1045 cm^{-1} is caused by the C–O–C group of the sugar structure in BS [28]. For BSC, 3ZF5-BSC, and 3ZF5-BSCH, the stretching vibration of –OH migrates to around 3414 cm^{-1} due to the binding of Ca^{2+} to the hydroxyl and carboxyl groups in SA, proving the successful cross-linking modification [29]. In the spectrum of the three aerogels containing ZF5, the absorption peak of 1045 cm^{-1} broadens to a strong absorption band of 1750 − 1200 cm^{-1}, attributed to the absorption superposition of bending vibration of the hydroxyl group on the ZF5 surface and carboxyl C=O stretching vibration [30]. The peaks at 2336, 869, and 435 cm^{-1}, are assigned to the fermi resonance of –OH in BS with Zn–OH, the Zn–OH group vibration, and Zn–O stretching vibration, respectively [31, 32]. Compared with 3ZF5-BS and 3ZF5-BSC, the hydrophobic modified 3ZF5-BSCH exhibits a new peak belonging to the Si–O–Si symmetric stretching vibration at 781 cm^{-1}, and a higher intensity of the absorption edge of 1400−1200 cm^{-1}, causing the shape of the absorption band at 1750−1200 cm^{-1} less symmetrical, meaning the presence of Si-CH_3 group in 3ZF5-BSCH [33]. Figure 4b and c show that the water droplet on the surface of 3ZF5-BSCH is close to spherical with a contact angle of 130 ± 2.5°, indicating that 3ZF5-BSCH has good hydrophobicity.

The XPS measurement was conducted for the 3ZF5-BSCH composite aerogel. As presented in Fig. 5a, the 3ZF5-BSCH composite aerogel mainly contains C, O, Zn, Fe, Na, and Si elements. The standard binding energy of

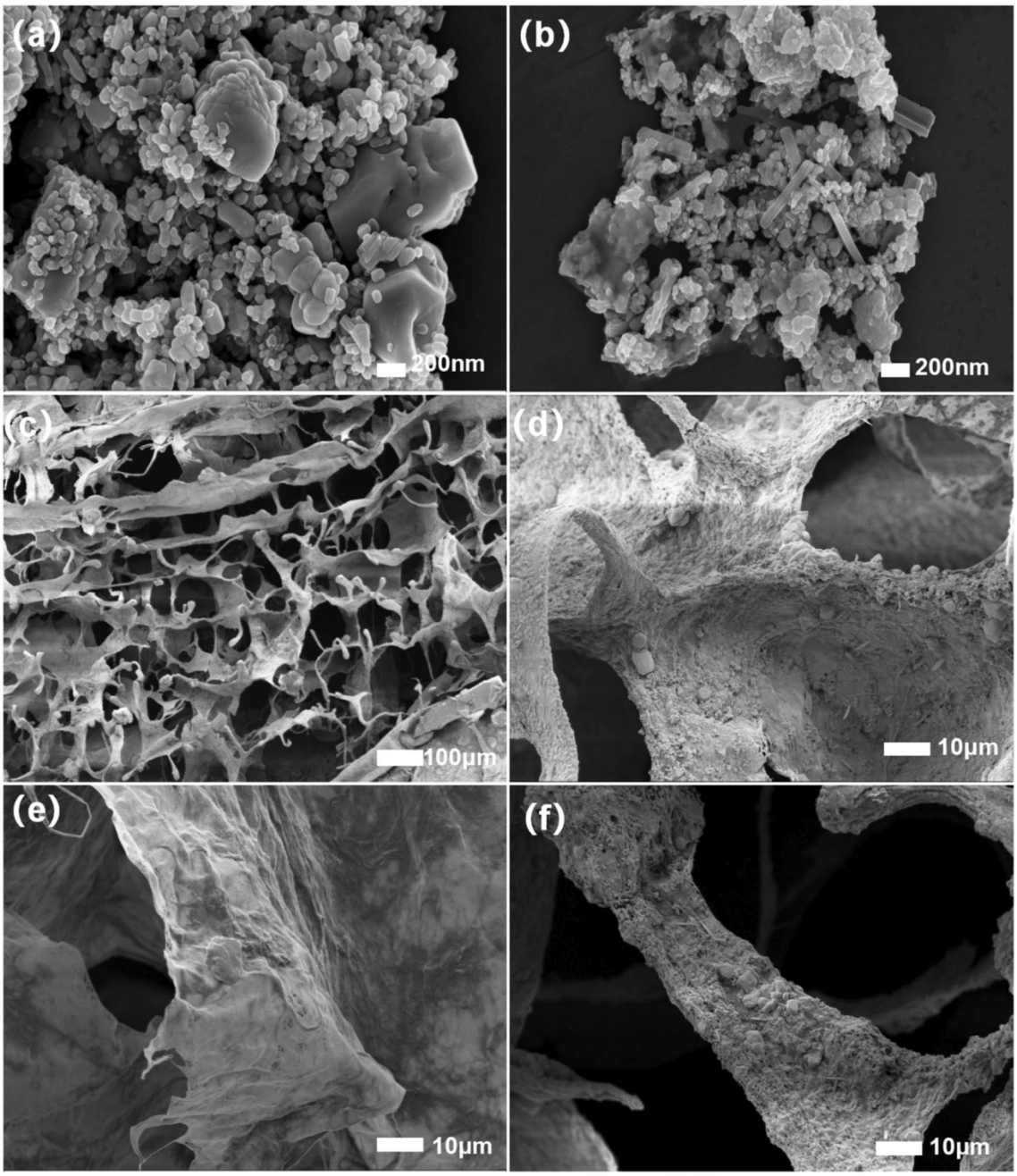

Fig. 3 SEM images of Z nanoparticles **a**, ZF5 nanoparticles **b**, 3ZF5-BSC composite aerogel **c**, **d**, BS aerogel **e**, 3ZF5-BSCH composite aerogel **f**

C 1s = 284.80 eV was used for the charge correction [34]. Figure 5b shows the C 1s spectrum can be fitted with three peaks, which may be assigned to C-C (284.78 eV), C-Si (286.34 eV), and C=O (289.71 eV), respectively [35]. In Fig. 5c, the strong peaks at 1021.34 eV and 1044.31 eV respectively correspond to the binding energies of Zn $2p_{3/2}$ and Zn $2p_{1/2}$, indicating the presence of Zn^{2+} in 3ZF5-BSCH [36, 37]. Figure 5d shows the Fe $2p_{3/2}$ and Fe $2p_{1/2}$ signals at 710.08 eV and 723.84 eV, respectively, and a satellite signal at 717.78 eV, which are consistent with the values reported for γ-Fe_2O_3 [38]. These findings strongly indicate that the iron ion kept its trivalent state in 3ZF5-BSCH. In Fig. 5e, the O 1s spectrum is fitted with four peaks, respectively, corresponding to the bonding states of oxygen in Zn–O (530.69 eV), C=O (531.85 eV), Si–O (532.94 eV), and the chemisorption of oxygen on the surface (535.74 eV) [39–42]. The results demonstrate the successful silanization of 3ZF5-BSCH aerogel.

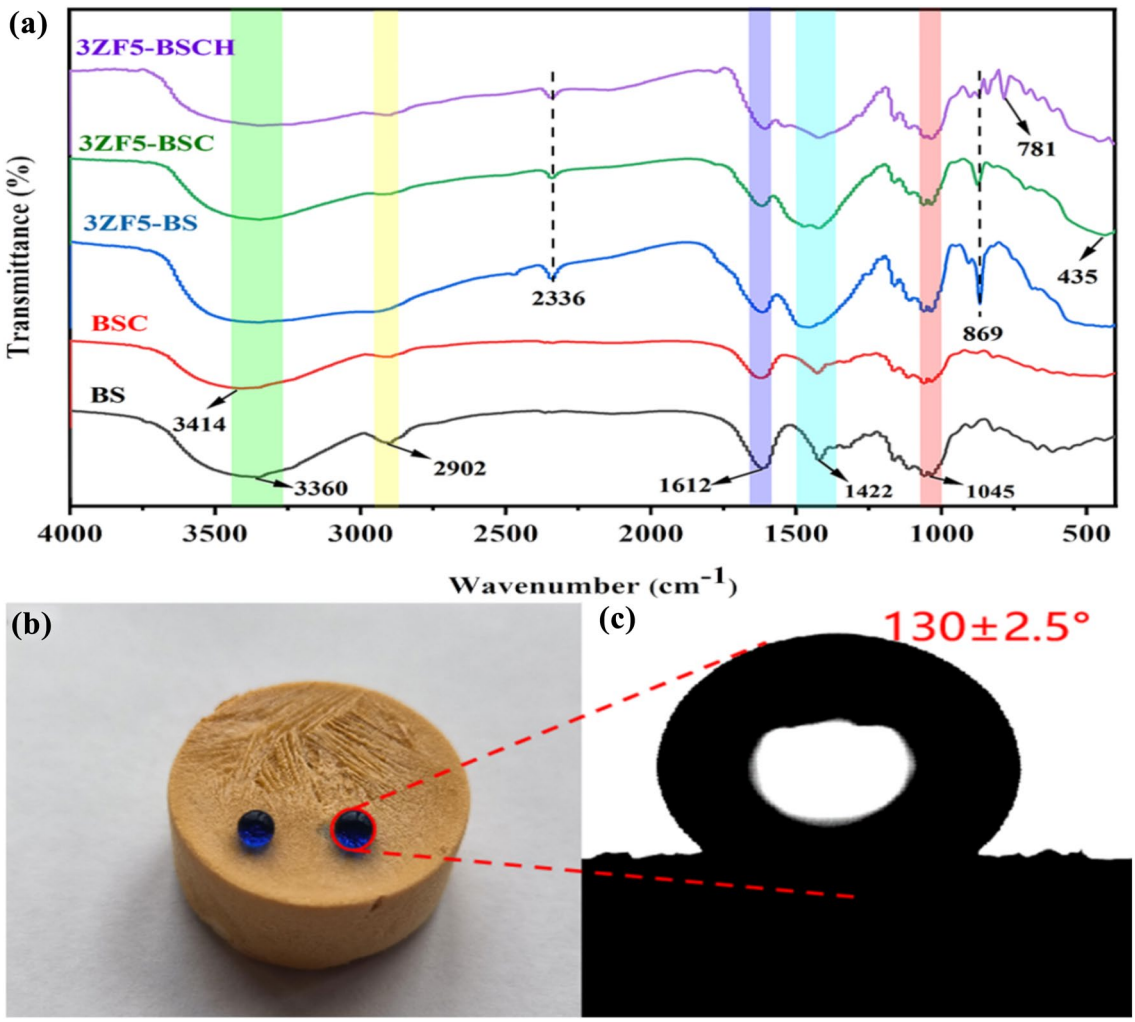

Fig. 4 **a** FT-IR spectra of the prepared samples. **b** The shape of a water droplet and **c** the contact angle of water on the surface of 3ZF5-BSCH

All the Fe-doped ZnO samples have a yellow tint, while pure ZnO is light grey. Figure 6a. shows the UV–Vis diffuse reflectance spectra of ZnO and Fe-doped ZnO samples. It can be seen that pure ZnO has strong absorption in the UV region, but almost no absorption in the visible region. Compared with ZnO, all the Fe-doped ZnO samples exhibit an enhanced UV-light response with the absorption edge red-shifted to the visible region. And with the increase of Fe^{3+} content, the absorption intensity gradually increases in the range of 400–550 nm (violet-green region). Among the four Fe-doped ZnO samples, ZF10 shows the highest absorption intensity in the violet-green region, while ZF5 has the highest absorption intensity in the yellow-red region. The 3ZF5-BSCH aerogel shows a higher absorption intensity in the yellow-red region compared to ZF5, indicating enhanced visible-light response via ZF5 compounded with BS aerogel.

The energy band gap value for Fe-doped ZnO nano-powder was determined using the Tauc plot method, as described by the formula [43]:

$$(\alpha h\nu)^{1/n} = A(h\nu - Eg) \tag{3}$$

where α is the absorption index: 2.303, h is Planck constant: 6.63 × 10–34 J·S, ν is frequency, A is constant, Eg is the semiconductor band gap, and ZnO is a direct band gap semiconductor: $n = 1/2$.

Figure 6b depicts the relationship between $(\alpha h\nu)^2$ and photon energy (hν). The energy band gap values are as follows: Z (3.17 eV), ZF1 (3.12 eV), ZF3 (3.06 eV), ZF5 (3.01 eV), and ZF10 (2.97 eV). The Fe^{3+} ion forms impurity energy level in the band gap near the conduction band edge and narrows the band gap of ZnO, leading to reduced excitation energy. Therefore, doping Fe^{3+} can effectively improve the visible-light response of ZnO.

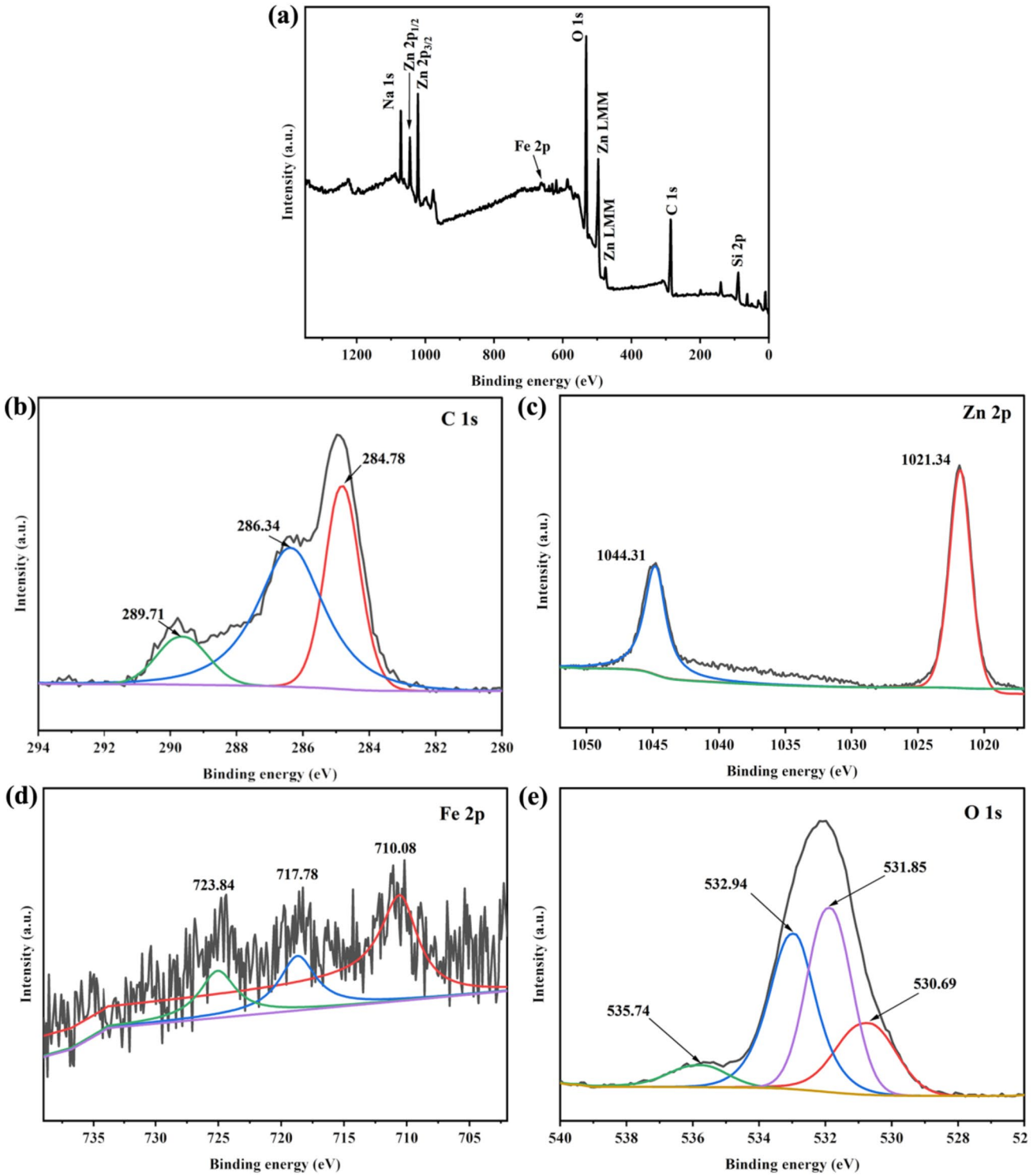

Fig. 5 XPS spectra of 3ZF5-BSCH aerogel: survey spectrum **a**, C 1s spectrum **b**, Zn 2p spectrum **c**, Fe 2p spectrum **d**, and O1s spectrum **e**

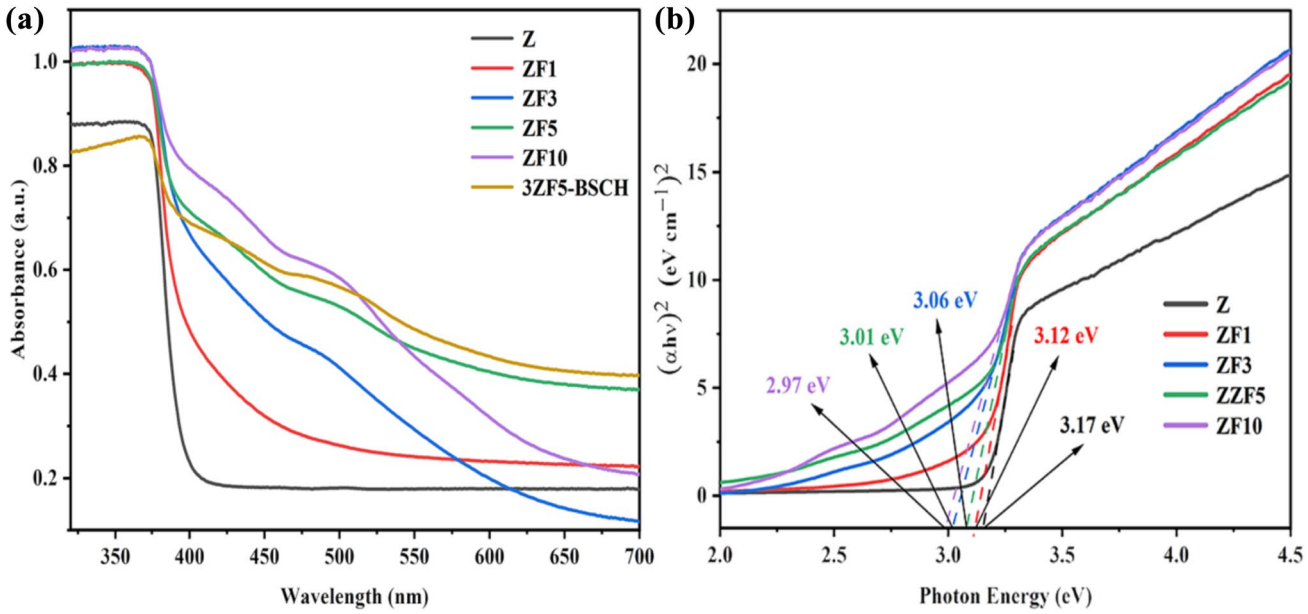

Fig. 6 **a** UV–Vis absorption spectra; **b** Tauc plot diagram of Z, ZF1, ZF3, ZF5, ZF10

The Effects of Crosslinking and Hydrophobic Modifications

The ZF5-BS aerogel has a strong power of water absorption, but its mechanical strength is insufficient to resist the swelling force of water, resulting in breakage and limited application. Furthermore, the aerogel would sink slowly as incoming water gradually fills its pores, resulting in less light harvested. Therefore, as a photocatalyst carrier, the composite aerogel is required to have excellent mechanical strength and floatability. Here, Ca^{2+} crosslinking and hydrophobic modifications are introduced to improve the strength of the aerogel skeleton, as well as make the aerogel floatable persistently.

Figure 7a shows the compressive stress-strain curves of 3FZ5-BS, 3FZ5-BSC, and 3FZ5-BSCH. It can be seen that the Ca^{2+} crosslinked aerogel (3ZF5-BSC) exhibits higher stress than the original aerogel (3FZ5-BS) in the strain range of 20–80%, suggesting that crosslinking can improve the mechanical strength of the aerogel. Under the same strain, the crosslinked and hydrophobically modified aerogel (3FZ5-BSCH) shows the highest stress, proving that the

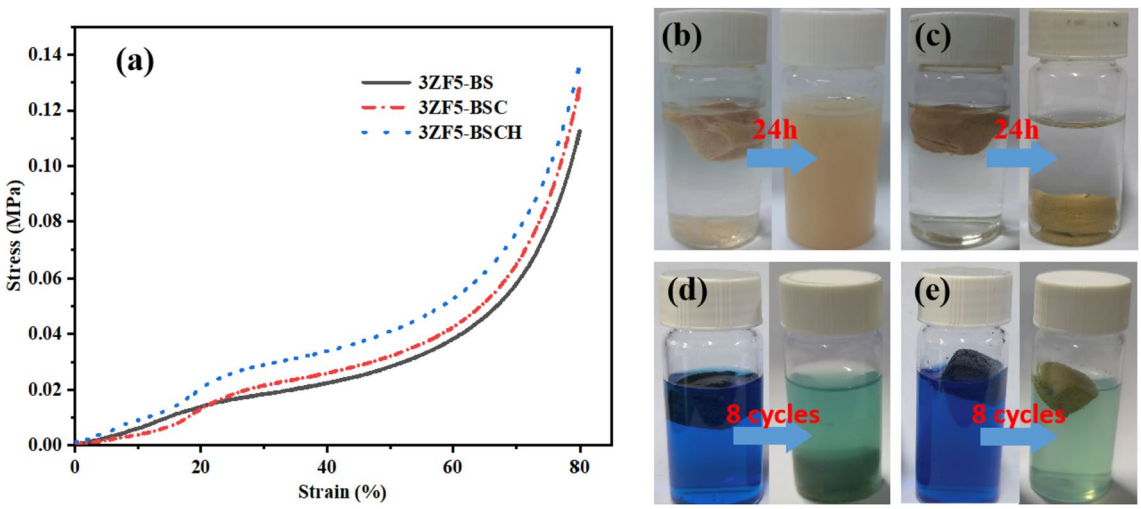

Fig. 7 **a** Compressive stress-strain curves of 3ZF5-BS, 3ZF5-BSC, and 3ZF5-BSCH; the comparison of ZF5-BS **b** and ZF5-BSC **c** after oscillating for 24 h, ZF5-BSC **d** and ZF5-BSCH **e** after 8 photocatalytic degradation cycles

strength of the aerogel is further improved through hydrophobic modification. Compared with 3ZF5-BS, the stresses of 3FZ5-BSC and 3FZ5-BSCH are increased by 13.2% and 44.9% at 50% strain, respectively. It can be explained as follows. SA contains many hydroxyl and carboxyl groups, which can be bonded with BC by hydrogen bonding interaction. On the other hand, the Ca^{2+} ion can replace the Na^{+} ion and coordinate with $–COO^{-}$ groups and OH^{-} in SA chains to form a more stable cross-linked network structure [29, 44]. Furthermore, the hydrophobic modifier MTMS contains three hydrolyzable alkoxy groups and one nonhydrolyzable methyl group. The silanol groups from the hydrolyzed MTMS could be easily polycondensed with the hydroxyl groups in BS aerogel, strengthening the aerogel network due to the insertion of the inorganic unit -Si-O-$SiCH_3$.

The effects of Ca^{2+} crosslinking and hydrophobic modifications were further demonstrated by a simple test. As shown in Fig. 7b, c, 3ZF5-BS, and 3ZF5-BSC were oscillated in deionized water at the speed of 200 r/min for 24 h, and the changes in the aerogel appearance were observed. It can be seen that the 3ZF5-BS aerogel without crosslinking has disintegrated into debris, while the crosslinked 3ZF5-BSC aerogel still maintains its original block shape. As shown in Fig. 7d, e shows the appearance of 3ZF5-BSC and 3ZF5-BSCH undergoing 8 cycles of photocatalytic degradation. After reaching the adsorption-desorption equilibrium, both the two aerogels can float in the MB solution to proceed with the photodegradation cycling experiment. However, after 8 cycles of photodegradation, the 3ZF5-BSC aerogel without hydrophobic modification sinks to the bottom and shows a partially broken shape, while the hydrophobic-modified aerogel 3ZF5-BSCH still floats in the MB solution and remains an intact shape. The hydrophobic modification can not only strengthen the aerogel but also keep its shape stable and floating state [45]. These results indicate that the combined crosslinking and hydrophobic modification is more effective than the single Ca^{2+} crosslinking modification for application in cycling photodegradation.

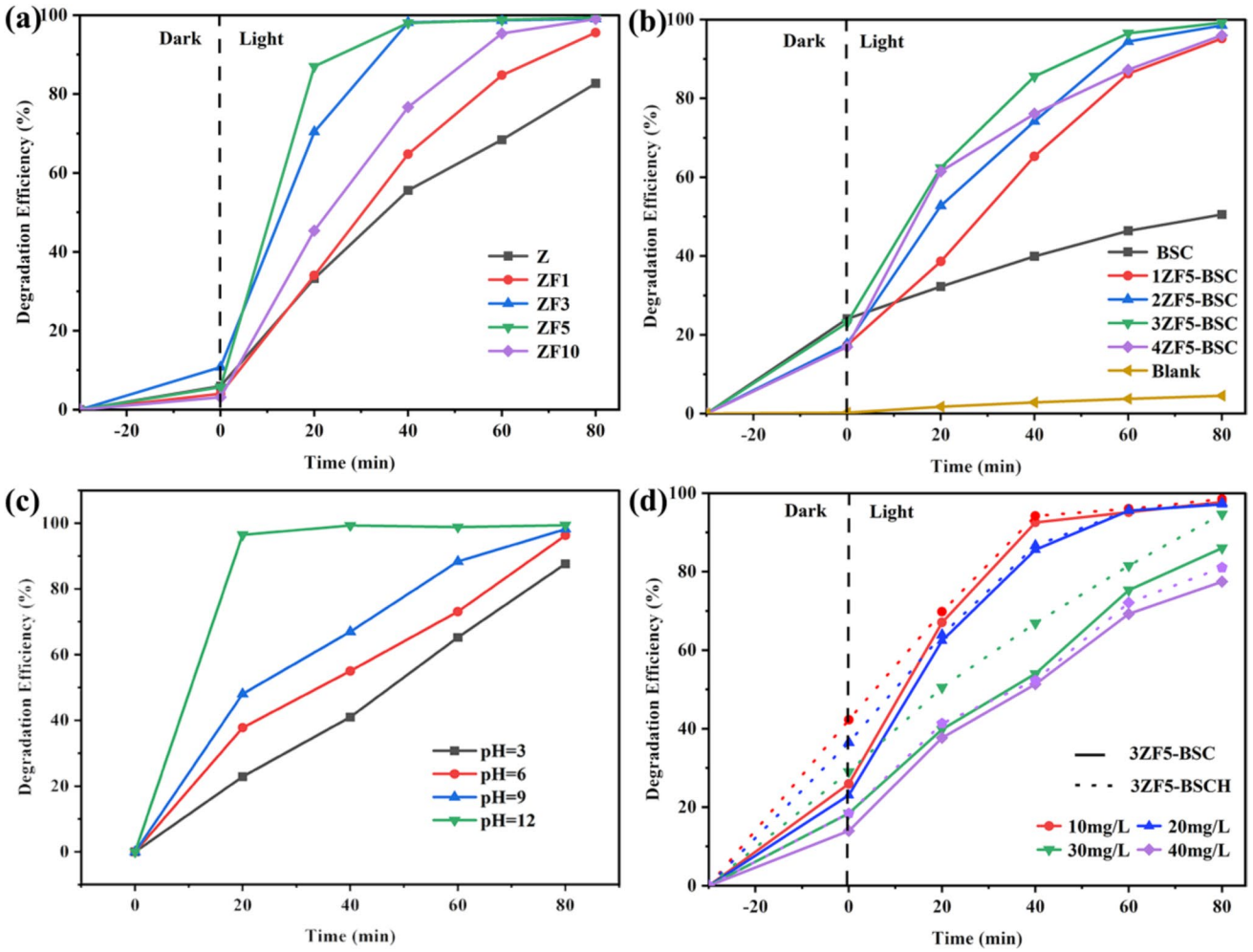

Fig. 8 Photocatalytic degradation curves of MB by ZnO doped with different Fe content **a**, ZF5-BSC with different ZF5 amount **b**, 3ZF5-BSC under different pH **c**, 3ZF5-BSC and 3ZF5-BSCH at different MB concentrations **d**

Photocatalytic Degradation Performance Analysis

The optimum Fe content is determined according to the photocatalytic efficiencies of Fe-doped ZnO to MB. Figure 8a presents the photocatalytic degradation efficiency versus irradiation time. After being irradiated for 20 min, samples Z, ZF1, ZF3, ZF5, and ZF10 exhibit photocatalytic degradation efficiencies of 33.3%, 34.0%, 70.4%, 87.0%, and 45.4%, respectively. As the irradiation time increases to 40 min, MB is almost completely degraded for samples ZF3, and ZF5. Therefore, the optimum Fe^{3+} content is determined to be 5 mol%, and ZF5 is chosen for reusable Fe-doped ZnO/BC/SA composite aerogel.

The effect of the ZF5 dosage on the photocatalytic activities of the crosslinked ZF5-BSC composite aerogels is evaluated by the photodegradation of MB under visible light. For comparison, the self-degradation efficiency of MB, and the absorbability of the crosslinked BSC aerogel without loading ZF5 are also investigated under simulated visible light. As shown in Fig. 8b, only 4.6% of MB undergoes self-degradation after 80 min of light exposure, indicating that MB is relatively stable. The BSC aerogel has a removal rate of 50.5% to MB, attributing to the adsorption of aerogel, while all the ZF5-BSC composite aerogels exhibit a high degradation efficiency (> 95%) owing to the presence of photocatalyst ZF5. The 4ZF5-BSC composite aerogel with the highest amount of ZF5 shows the fastest MB photodegradation rate during the first 20 min of irradiation. However, after being irradiated for 20 to 60 min, the 4ZF5-BSC composite aerogel shows minimal MB degradation activity. It can be explained that the aggregation of photocatalyst particles may occur with increasing amounts of ZF5 in ZF5-BA aerogel, tending to increase the recombination rate of electron-hole pairs when the concentration of the photogenerated electrons and holes increase to a certain extent, and consequently degrading the photocatalytic performance. From Fig. 8b, it can also be observed that the 3ZF5-BSC composite aerogel exhibits the highest degradation efficiency of 97.2% for MB after being irradiated for 80 min. Therefore, the optimum mass ratio of ZF5 to BS precursor is determined to be 3:100, and the 3ZF5-BSC composite aerogel is chosen for subsequent crosslinked and hydrophobically modification. It seems that the 3ZF5-BSC composite aerogel has a slightly lower photodegradation activity compared to ZF5. Considering the fact that the mass of ZF5 in 3ZF5-BSC (75 mg) is only three-quarters of that of ZF5 powder (100 mg) used for photocatalytic experiment, it can be inferred that the photocatalytic activity of the ZF5 catalyst is almost unchanged after compounded with the BC/SA aerogel.

The pH of the solution is a crucial factor influencing the photocatalytic degradation of dyes, because the concentration of hydroxyl radicals on MB dye molecules, the adsorption-desorption of dye molecules and their intermediates on the photocatalyst surface, and the photocatalyst's surface charge properties are all affected by the pH value of the dye solution. The initial pH value of the MB solution (20 mg/L) was gradually adjusted from 7.8 to 3, 6, 9, and 12 using 0.1 M HCl and 0.1 M NaOH solutions, and the effect of pH on the degradation efficiency of 3ZF5-BSC to MB is shown in Fig. 8c. It can be seen that the degradation efficiency increases with pH value. Due to the cationic dye nature of MB, alkaline conditions would promote more MB dye molecules on the surface of the photocatalyst to facilitate the photodegradation reaction of MB, while acidic conditions would lead to fewer MB molecules on the surface of the photocatalyst due to the presence of the competitive adsorption between H^+ and MB molecules. After irradiated 80 min, the degradation efficiencies for pH = 3, 6, and 9 are 87.6%, 96.3%, and 98.2%, respectively. In the case of pH = 12, the degradation efficiency is as high as 96.4% even after irradiation for 20 min.

Figure 8d shows the photocatalytic activities of 3ZF5-BSC and 3ZF5-BSCH composite aerogels at different initial MB concentrations. For both aerogels, it can be observed that the degradation efficiency decreases gradually with increasing MB concentration because the ZF5 photocatalyst with constant mass cannot provide sufficient reactive sites for the additional MB molecules in the solution. On the other hand, the turbidity of the solution increases with initial MB concentration, leading to decreased visible light transmittance and consequently reduced photogenerated electrons concentration and photocatalytic degradation efficiency. In the dark, benefiting from its excellent hydrophobicity, 3ZF5-BSCH shows a much higher adsorption ability to MB than 3ZF5-BSC. Under visible light, 3ZF5-BSCH shows a higher MB degradation efficiency than 3ZF5-BSC, and its superiority is more obvious at high initial concentrations of 30 and 40 mg/L. After irradiated 80 min, the degradation efficiencies at initial concentrations of 10, 20, 30, and 40 mg/L are 97.7%, 97.2%, 86.0%, and 77.4% for 3ZF5-BSC, and 98.5%, 97.4%, 94.7% and 81.0% for 3ZF5-BSCH, respectively. The results suggest that the combined modified 3ZF5-BSCH composite aerogel can maintain a high degradation efficiency at an initial concentration of 10–40 mg/L, showing a good application prospect in the degradation of MB.

The kinetic behaviors of 3ZF5-BSC and 3ZF5-BSCH during the photodegradation of MB are further studied according to the pseudo-first-order model: $\ln(C_0/C) = Kt$, where t, K, C_0, C is the irradiation time (min), the rate constant, the MB concentration at t = 0 and time t, respectively [45. Figure 9 shows the plots of $-\ln(C/C_0)$ vs. time at

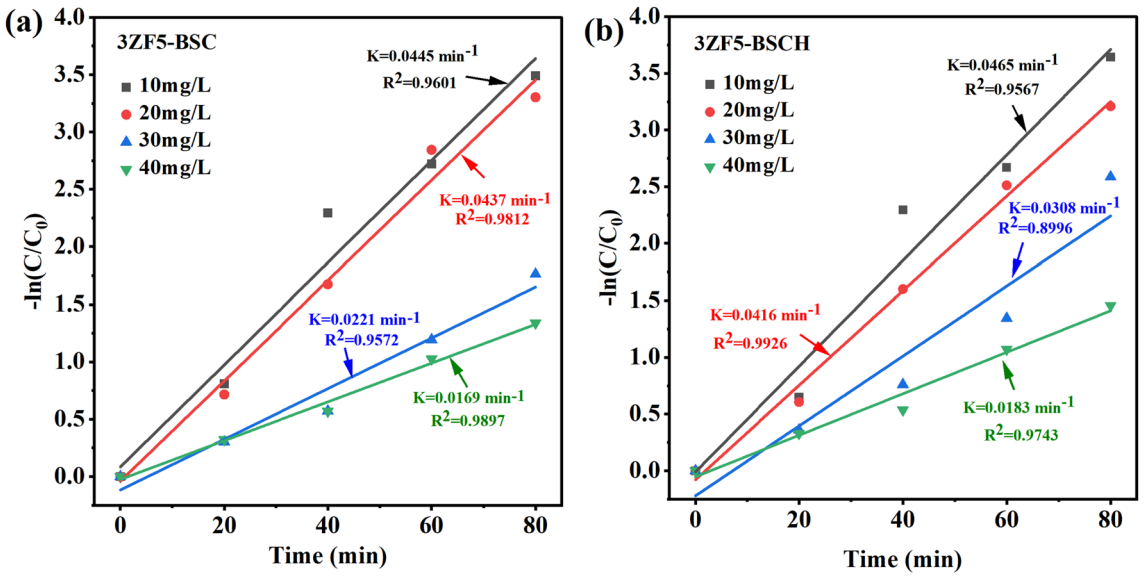

Fig. 9 The linear fitting curves of the pseudo-first-order model for 3ZF5-BSC **a** and 3ZF5-BSCH **b**

different initial MB concentrations. The graph is fitted linearly and the slope represents the rate constant K. Except for the case of 3ZF5-BSCH at 30 mg/L, the correlation coefficient R^2 in other cases is not lower than 0.9567, suggesting the validity of the pseudo-first-order model. As the initial MB concentration increases from 10 mg/L to 40 mg/L, the rate constant of 3ZF5-BSC decreases from 0.0445 min^{-1} to 0.0169 min^{-1} (Fig. 9a), and the rate constants 3ZF5-BSCH decreases from 0.0465 min^{-1} and 0.0183 min^{-1} (Fig. 9b), indicating an improved photocatalytic activity of 3ZF5-BSCH.

Photocatalytic Cycle Performance Analysis

The excellent stability of photocatalytic performance is crucial for the long-term use of the prepared composite aerogel. As shown in Fig. 10a, cycling experiments were conducted using 3ZF5-BSC and 3ZF5-BSCH for the degradation of MB, and the photocatalytic degradation of MB during 8 cycles was compared. It can be observed that the degradation efficiencies of MB by 3ZF5-BSC and 3ZF5-BSCH gradually decrease with increasing cycles, but the decline rate of degradation efficiency for 3ZF5-BSCH is significantly

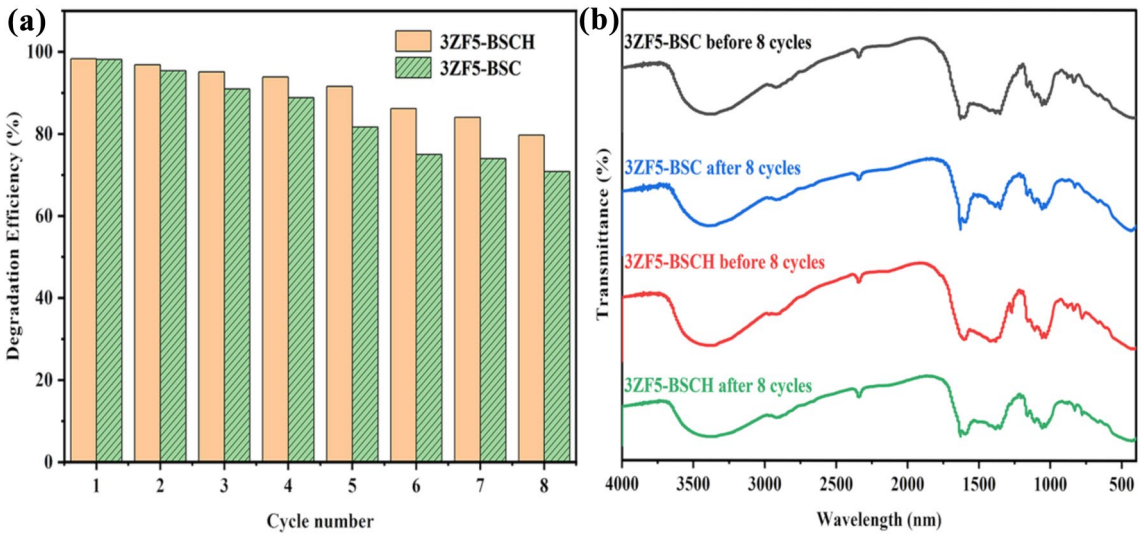

Fig. 10 Cycle degradation efficiency of MB with 3ZF5-BSC and 3ZF5-BSCH under visible-light irradiation **a** and the FT-IR spectra of the aerogels before and after 8 cycles **b**

lower than that for 3ZF5-BSC. Thanks to its hydrophobicity, 3ZF5-BSCH can keep floating throughout every cycling process, conversely, 3ZF5-BSC without hydrophobic modification will gradually sink to the bottom after prolonged immersion. Consequently, in the case of 3ZF5-BSCH, a higher intensity of illumination occurs, evoking an enhanced photocatalytic efficiency compared with 3ZF5-BSC. The degradation efficiencies of MB by 3ZF5-BSC and 3ZF5-BSCH are 88.8% and 93.8% after the 4th degradation cycle, 70.8% and 79.7% after the 8th degradation cycle, respectively. Considering that in the cycling process, the recycled composite aerogel is wiped with paper before being used for the next cycle, only the solution on the surface has been removed and there is still some residual MB solution inside. Thus, the actual cycling degradation rate is inferred to be higher than the measured value. Figure 10b shows that the FT-IR spectra of 3ZF5-BSC and 3ZF5-BSCH are almost unchanged after 8 cycles, indicating that the structures of 3ZF5-BSC and 3ZF5-BSCH remained stable after multiple cycles. These results signify that the composite aerogel undergoing crosslinking and hydrophobic modifications exhibits excellent stability of photocatalytic performance, showing its practical application prospect.

Table 2 shows a comparison of the photodegradation activity and stability between 3ZF5-BSCH and some reported photocatalysts, including Fe-doped ZnO/cellulose nanocomposite [13] and some aerogel-based photocatalyst composites [24, 45, 46]. It can be seen that, even without

Table 2 The photodegradation performance of 3ZF5-BSCH and some reported photocatalysts

Photocatalyst	dosage (mg)	Light power(W) /Time (min)	C(mg/L)/V (mL) /pH	η(%)	Cyclic η(%) /number	Refs.
FeZnO/cellulose nanocomposite	100	visible [a] 250 /120	5/100/9	98.84	92.31/5	[13]
Ag_2O/Zwitterionic BC aerogel	50	visible [b] 300 /180	5/50/NA	96.59	94.47/6	[24]
cellulose carbon aerogel@$Na_2Ti_3O_7$@ Cu_2O nanocomposite	200	sunny light -- /120	5/300/11	99	92.4/5	[45]
			20/300/11	97.5	–	
microcrystalline cellulose/Cu_2O/ graphene oxide composite foam	200	visible [b] --/60	20/40/NA	77.9	41.1/5	[46]
FeZnO/BC/SA composite aerogel	110	visible [b] 300 /80	20/20/NA	97.4	93.8/4 79.7/8	This work
			30/20/NA	94.7	–	

a: high-pressure mercury lamp with a cut filter (< 400 nm)

b: Xe lamp with a cut filter (< 420 nm)

NA: non-adjusted pH

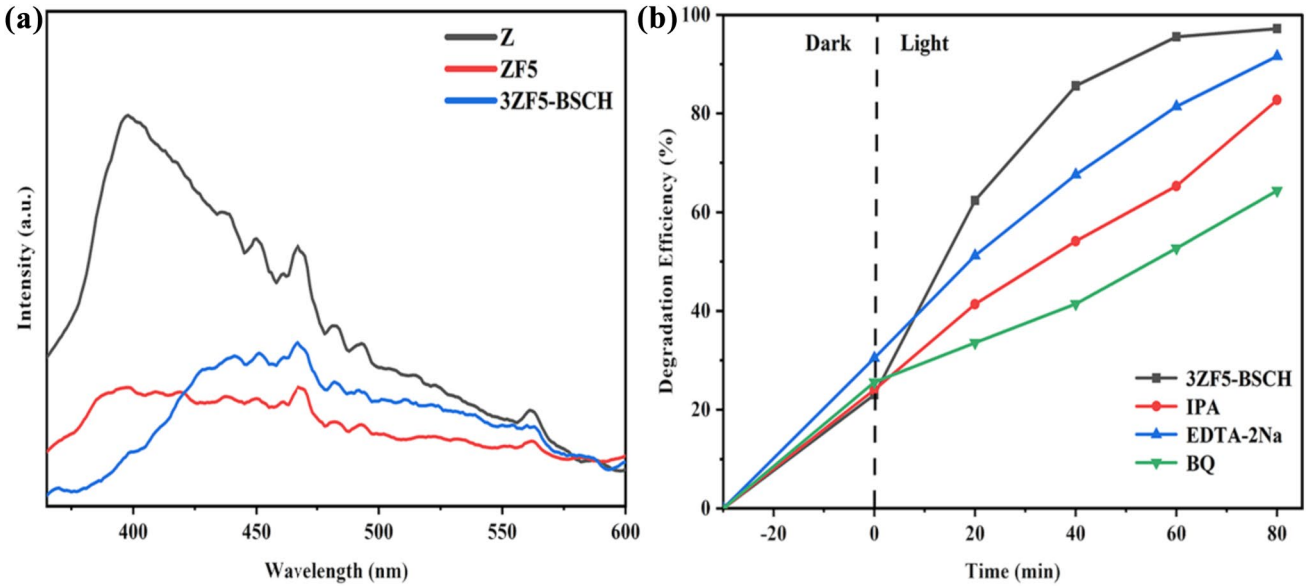

Fig. 11 PL spectra of Z, ZF5, and 3ZF5-BSCH **a** and effect of radicals on MB degradation with 3ZF5-BSCH **b**

adding a pH regulator, 3ZF5-BSCH exhibits a superior or competitive degradation efficiency and satisfactory degradation stability. Therefore, the prepared composite aerogel in this work is a promising candidate for MB degradation.

Synergistic Photocatalytic Degradation Mechanism

Figure 11a shows the PL spectra of Z, ZF5, and 3ZF5-BSCH. All the samples show a wide emission peak between 350 and 500 nm, which is attributed to the near-band edge emission of ZnO resulting from the combination of electron-hole pairs. The PL intensity of ZF5 is much lower than that of Z, suggesting ZF5 exhibits a lower electron-hole recombination rate. In the Fe^{3+}-doped ZnO lattice, there are a few zinc vacancies due to the unequal-valent substitution between Fe^{3+} and Zn^{2+}. The vacancies and the Fe^{3+} ions can trap the photogenerated holes and electrons, respectively, which suppresses the electron-hole pairs recombination and results in enhanced photocatalytic activity of ZF5. From Fig. 11a, it can also be observed that the PL intensity of 3ZF5-BSCH is higher than that of ZF5 slightly, suggesting the combination of ZF5 and BSCH can keep the effective separation of electron-hole pairs [47].

Various scavengers were introduced in the 3ZF5-BSCH photocatalytic system to evaluate the role of active species in the photocatalytic degradation reaction. EDTA-2Na (0.1 mmol/L), BQ (0.1 mmol/L) and IPA (0.1 mmol/L) were used as quenching agents for photogenerated holes (h^+), superoxide radicals ($\cdot O^{2-}$), and hydroxyl radicals ($\cdot OH$), respectively. As shown in Fig. 11b, the degradation efficiency of MB decreases from 97.17 to 91.61%, 82.74%, and 64.35% when EDTA-2Na, IPA, and BQ are added, respectively. These results reveal the primacy role of $\cdot O^{2-}$ in the photocatalytic degradation reaction. Furthermore, the role order is elucidated as follows: $\cdot O^{2-} > \cdot OH > h^+$.

MB can be continuously adsorbed and efficiently degraded throughout the photocatalytic degradation process in 3ZF5-BSCH system. The excellent degradation efficiency is ascribed to the effective separation of electron-hole pairs, strong visible-light response and highly porous structure of 3ZF5-BSCH composite aerogel. As shown in Fig. 12, a possible synergistic photocatalytic mechanism is proposed here. For the 3ZF5-BSCH after visible light irradiation, electrons of ZF5 undergo transitions from the valence band (VB) to the conduction band (CB), generating reducing electrons (e^-) in VB and oxidizing holes (h^+) in CB. These photogenerated electron-hole pairs can be separated effectively due to the existence of Fe^{3+} ions and zinc vacancies. The holes accumulated on the surface can readily react with water to generate hydroxyl radicals ($\cdot OH$), while the reducing electrons can react with the adsorbed or dissolved oxygen to form superoxide radical anions ($\cdot O^{2-}$). Finally, the MB molecules react with $\cdot OH$ and $\cdot O^{2-}$ to degrade into CO_2 and H_2O. The key reaction process for the degradation of MB is given in Eqs. (4–8):

$$3ZF5 - BSCH + h\nu \rightarrow e^- + h^+ \quad (4)$$

$$e^- + O_2 \rightarrow \cdot O_2^- \quad (5)$$

$$h^+ + H_2O \rightarrow \cdot OH \quad (6)$$

$$\cdot OH + MB \rightarrow CO_2 + H_2O \quad (7)$$

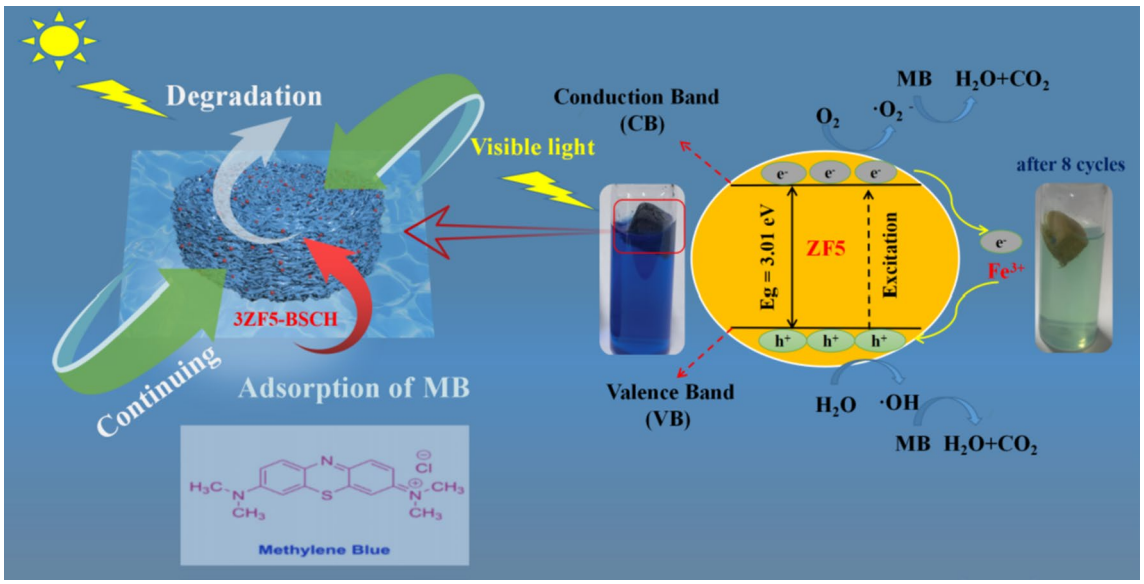

Fig. 12 Photocatalytic degradation mechanism of 3ZF5-BSCH

$$\cdot O_2^- + MB \rightarrow CO_2 + H_2O \quad (8)$$

4. Conclusions

In this work, a novel and floatable Fe-doped ZnO/BC/SA composite aerogel with excellent visible-light-driven degradation performance and recyclability has been successfully synthesized via freeze-drying and combined modifications. The optimal mass ratio of ZF5 to BS precursor is determined to be 3:100. Doping Fe^{3+} can improve the visible-light response of ZnO and promote the separation of electrons and holes, resulting in efficient degradation of MB. The combination of crosslinking and hydrophobic modifications not only reinforces the BC/SA aerogel backbone significantly but also makes the aerogel steady floating, endowing excellent cycling photocatalytic performance. The floating 3ZF5-BSCH aerogel exhibits a degradation efficiency of 79.7% even after 8 cycles, showing great potential in visible-light-driven degradation of MB. This research can provide new prospects for exploring aerogel-like composites with excellent visible light photocatalytic performance.

Acknowledgements This work is financially supported by the Fujian Provincial Nature Science Foundation of China (Grant 2018J01755).

Author Contributions Xiangqi Li: Supervision, Review and Funding. Xutao Zhang: Material preparation; Experimental design; Data processing and writing. Weiliang Chen: Material preparation; Methodology, Introduction and Review.

Declarations

Competing Interests The authors declare no competing interests.

Ethical Approval Not applicable.

References

1. Katheresan V, Kansedo J, Lau SY (2018) Efficiency of various recent wastewater dye removal methods: a review. J Environ Chem Eng 6(4):4676–4697. https://doi.org/10.1016/j.jece.2018.06.060
2. Vikrant K, Giri BS, Raza N, Roy K, Kim K-H, Rai BN, Singh RS (2018) Recent advancements in bioremediation of dye: current status and challenges. Bioresour Technol 253:355–367. https://doi.org/10.1016/j.biortech.2018.01.029
3. Elfeky AS, Salem SS, Elzaref AS, Owda ME, Eladawy HA, Saeed AM, Awad MA, Abou-Zeid RE, Fouda A (2020) Multifunctional cellulose nanocrystal /metal oxide hybrid, photo-degradation, antibacterial and larvicidal activities. Carbohydr Polym 230:115711. https://doi.org/10.1016/j.carbpol.2019.115711
4. Celik S, Duman N, Sayin F, Tunali Akar S, Akar T (2021) Microbial cells immobilized on natural biomatrix as a new potential ecofriendly biosorbent for the biotreatment of reactive dye contamination. J Water Process Eng 39:101731. https://doi.org/10.1016/j.jwpe.2020.101731
5. Xue Y, Kamali M, Zhang X, Askari N, De Preter C, Appels L, Dewil R (2023) Immobilization of photocatalytic materials for (waste) water treatment using 3D printing technology–advances and challenges. Environ Pollut 316:120549. https://doi.org/10.1016/j.envpol.2022.120549
6. Tang L, Yu J, Pang Y, Zeng G, Deng Y, Wang J, Ren X, Ye S, Peng B, Feng H (2018) Sustainable efficient adsorbent: alkali-acid modified magnetic biochar derived from sewage sludge for aqueous organic contaminant removal. Chem Eng J 336:160–169. https://doi.org/10.1016/j.cej.2017.11.048
7. Liu J, Wang H, Li WJ, Xie HX, Li X, Yang LQ, Song SJ (2023) Controllable fabrication of $Bi_4Ti_3O_{12}$/C/Bi_2S_3/MoS_2 heterojunction with effective suppression of Bi_2S_3 assisted by amorphous carbon interlayer for significantly enhanced photocatalysis. J Taiwan Inst Chem Eng 146:104882. https://doi.org/10.1016/j.jtice.2023.104882
8. Kim D, Yong K (2021) Boron doping induced charge transfer switching of a C_3N_4/ZnO photocatalyst from Z-scheme to type ii to enhance photocatalytic hydrogen production. Appl Catal B 282:119538. https://doi.org/10.1016/j.apcatb.2020.119538
9. Türkyılmaz ŞŞ, Güy N, Özacar M (2017) Photocatalytic efficiencies of Ni, Mn, Fe and Ag doped ZnO nanostructures synthesized by hydrothermal method: the synergistic/antagonistic effect between ZnO and metals. J Photochem Photobiol A 341:39–50. https://doi.org/10.1016/j.jphotochem.2017.03.027
10. Young SJ, Liu YH, Chien JT (2018) Improving field electron emission properties of ZnO nanosheets with ag nanoparticles adsorbed by photochemical method. ACS Omega 3(7):8135–8140. https://doi.org/10.1021/acsomega.8b01041
11. Sharma M, Poddar M, Gupta Y, Nigam S, Avasthi DK, Adelung R, Abolhassani R, Fiutowski J, Joshi M, Mishra YK (2020) Solar light assisted degradation of dyes and adsorption of heavy metal ions from water by CuO-ZnO tetrapodal hybrid nanocomposite. Mater Today Chem 17:100336. https://doi.org/10.1016/j.mtchem.2020.100336
12. Kouhail M, El Ahmadi Z, Benayada A (2022) Effect of Ag, ca, and Fe on photocatalytic activity of ZnO nanoparticles to remove textile dyes under sunlight irradiation. React Kinet Mech Catal 135(1):169–182. https://doi.org/10.1007/s11144-021-02061-1
13. Vasheghani F, Mohammad S, Nikzad M, Ghorbani M (2022) Fabrication of Fe-doped ZnO /nanocellulose nanocomposite as an efficient photocatalyst for degradation of methylene blue under visible light. Cellulose 29(13):7277–7299. https://doi.org/10.1007/s10570-022-04735-y
14. Saeed M, Muneer M, Haq A, Akram N (2022) Photocatalysis: an effective tool for photodegradation of dyes-a review. Environ Sci Pollut Res 29(1):293–311. https://doi.org/10.1007/s11356-021-16389-7
15. Sekar AD, Muthukumar H, Chandrasekaran NI, Matheswaran M (2018) Photocatalytic degradation of naphthalene using calcined Fe ZnO / PVA nanofibers. Chemosphere 205:610–617. https://doi.org/10.1016/j.chemosphere.2018.04.131
16. Hasanpour M, Hatami M (2020) Photocatalytic performance of aerogels for organic dyes removal from wastewaters: review study. J Mol Liq 309:113094. https://doi.org/10.1016/j.molliq.2020.113094
17. Truong HB, Rabani I, Huy BT, Tran NHT, Hur J (2023) Using floating photocatalyst mpg-C_3N_4/expanded perlite to treat natural organic matter under visible light. Chem Eng J 466:143178. https://doi.org/10.1016/j.cej.2023.143178
18. Shah N, Ul-Islam M, Khattak WA, Park JK (2013) Overview of bacterial cellulose composites: a multipurpose advanced material. Carbohydr Polym 98(2):1585–1598. https://doi.org/10.1016/j.carbpol.2013.08.018

19. Kaushik M, Moores A (2016) Review: Nanocelluloses as versatile supports for metal nanoparticles and their applications in catalysis. Green Chem 18(3):622–637. https://doi.org/10.1039/C5GC02500A
20. Bergottini VM, Bernhardt D (2023) Bacterial cellulose aerogel enriched in nanofibers obtained from Kombucha Scoby byproduct. Mater Today Commun 35:105975. https://doi.org/10.1016/j.mtcomm.2023.105975
21. Ma H, Wang Z, Zhang X, Yao J (2023) Bimetallic MOF@bacterial cellulose derived carbon aerogel for efficient electromagnetic wave absorption. Ceram Int 49(12):20951–20959. https://doi.org/10.1016/j.ceramint.2023.03.228
22. Sun B, Zhao J, Wang T, Li YYang X, Tan F, Li Y, Chen C, Sun D (2023) Highly efficient construction of sustainable bacterial cellulose aerogels with boosting pm filter efficiency by tuning functional group. Carbohydr Polym 309:120664. https://doi.org/10.1016/j.carbpol.2023.120664
23. Pereira ALS, Feitosa JPA, Morais JPS, Rosa M, d F (2020) Bacterial cellulose aerogels: influence of oxidation and silanization on mechanical and absorption properties. Carbohydr Polym 250:116927. https://doi.org/10.1016/j.carbpol.2020.116927
24. Jiang J, Zhu J, Zhang Q, Zhan X, Chen F (2019) A shape recovery zwitterionic bacterial cellulose aerogel with superior performances for water remediation. Langmuir 35(37):11959–11967. https://doi.org/10.1021/acs.langmuir.8b04180
25. Štengl V, Popelková D, Vláčil P (2011) TiO_2-graphene nanocomposite as high performace photocatalysts. J Phys Chem C 115(51):25209–25218. https://doi.org/10.1021/jp207515z
26. Ciciliati MA, Silva MF, Fernandes DM, de Melo MAC, Hechenleitner AAW, Pineda, E A G (2015) Fe-doped ZnO nanoparticles: synthesis by a modified sol–gel method and characterizati on. Mater Lett 159:84–86. https://doi.org/10.1016/j.matlet.2015.06.023
27. Xiao H, Zhang W, Wei Y, Chen L (2018) Carbon/ZnO nanorods composites templated by tempo-oxidized cellulose and photocatalytic activity for dye degradation. Cellulose 25(3):1809–1819. https://doi.org/10.1007/s10570-018-1651-4
28. Kim JH, Park S, Kim H, Kim HJ, Yang YH, Kim YH, Lee SH (2017) Alginate/bacterial cellulose nanocomposite beads prepared using Gluconacetobacter xylinus and their application in lipase immobilization. Carbohydr Polym 157:137–145. https://doi.org/10.1016/j.carbpol.2016.09.074
29. Xu P, Song J, Dai Z, Xu Y, Li D, Wu C (2021) Effect of ca. crosslinking Prop Struct lutein-loaded Sodium Alginate Hydrogels Int J Biol Macromol 193:53–63. https://doi.org/10.1016/j.ijbiomac.2021.10.114
30. Chen S, Zhou B, Hu W, Zhang W, Yin N, Wang H (2013) Polyol mediated synthesis of ZnO nanoparticles templated by bacterial cellulose. Carbohydr Polym 92(2):1953–1195. https://doi.org/10.1016/j.carbpol.2012.11.059
31. Doan Thi TU, Nguyen TT, Thi YD, Ta Thi KH, Phan BT, Pham KN (2020) Green synthesis of ZnO nanoparticles using orange fruit peel extract for antibacterial activities. RSC Adv 10(40):23899–23907. https://doi.org/10.1039/D0RA04926C
32. Sohrabi S, Keshavarz Moraveji M, Iranshahi D, Karimi A (2022) Microfluidic assisted low-temperature and speedy synthesis of TiO_2/ZnO/GOx with bio/photo active cites for Amoxicillin degradation. Sci Rep 12(1):15488. https://doi.org/10.1038/s41598-022-19406-y
33. Yang X, Ma J, Ling J, Li N, Wang D, Yue F, Xu S (2018) Cellulose acetate-based SiO_2/TiO_2 hybrid microsphere composite aerogel films for water-in-oil emulsion separation. Appl Surf Sci 435:609–616. https://doi.org/10.1016/j.apsusc.2017.11.123
34. Li J, Hu C, Liu B, Liu Z (2023) Dual pathway reduction of Mo^{4+} and photogenerated electrons restore catalytic sites to enhance heterogeneous peroxymonosulfate activation system. Chem Eng J 452:139246. https://doi.org/10.1016/j.cej.2022.139246
35. Shen F, Chen C, Chen W, Liu Q, Chen C, Xiao G, Zhou J (2022) Ultra-light GO@ KGM aerogels for oil–water separation based on CVD modification. ACS Omega 7(15):13354–13361. https://doi.org/10.1021/acsomega.2c01080
36. Yang HY, Yu SF, Lau SP, Herng TS, Tanemura M (2009) Ultraviolet laser action in ferromagnetic Zn1-xFexO nanoneedles. Nanoscale Res Lett 5(1):247. https://doi.org/10.1007/s11671-009-9473-9
37. Patil SS, Mali MG, Tamboli MS, Patil DR, Kulkarni MV, Yoon H, Kim H, Al-Deyab SS, Yoon SS, Kolekar SS, Kale BB (2016) Green approach for hierarchical nanostructured Ag-ZnO and their photocatalytic performance under sunlight. Catal Today 260:126–134. https://doi.org/10.1016/j.cattod.2015.06.004
38. Yang Z, Zhong W, Au C, Du X, Song H, Qi X, Ye X, Xu M, Du Y (2009) Novel photoluminescence properties of magnetic Fe/ZnO composites: self-assembled ZnO nanospikes on Fe nanoparticles fabricated by hydrothermal method. J Phys Chem C 113(51):21269–21273. https://doi.org/10.1021/jp903130t
39. Xia C, Hu C, Tian Y, Chen P, Wan B, Xu J (2011) Room-temperature ferromagnetic properties of Fe-doped ZnO rod arrays. Solid State Sci 13(2):388–393. https://doi.org/10.1016/j.solidstatesciences.2010.11.041
40. Rambu AP, Nica V, Dobromir M (2013) Influence of Fe-doping on the optical and electrical properties of ZnO films. Superlattices Microstruct 59:87–96. https://doi.org/10.1016/j.spmi.2013.03.023
41. Choi H, Shin D, Yeo BC, Song T, Han SS, Park N, Kim S (2016) Simultaneously controllable doping sites and the activity of a W-N codoped TiO_2 photocatalyst. ACS Catal 6(5):2745–2753. https://doi.org/10.1021/acscatal.6b00104
42. Yi L, Yang J, Fang X, Xia Y, Zhao L, Wu H, Guo S (2020) Facile fabrication of wood-inspired aerogel from Chitosan for efficient removal of oil from Water. J Hazard Mater 385:121507. https://doi.org/10.1016/j.jhazmat.2019.121507
43. Fest A, Tristán F, Perez-Vigueras W, Labrada-Delgado GJ, Meneses-Rodríguez D, Vega-Díaz SM (2023) Metal decorated carbon nanotube aerogels from sodium polyacrylate crosslinking by divalent ions. Carbon Trends 10:100235. https://doi.org/10.1016/j.cartre.2022.100235
44. Yan Z, Zhu K, Li X, Wu X (2022) Recyclable bacterial cellulose aerogel for oil and water separation. J Polym Environ 30(7):2774–2784. https://doi.org/10.1007/s10924-021-02369-y
45. Liu Y (2023) Functional cellulose aerogel nanocomposites with enhanced adsorption capability and excellent photocatalytic performance. Int J Biol Macromol 231:123393. https://doi.org/10.1016/j.ijbiomac.2023.123393
46. Nie J, Li C, Jin Z, Hu W, Wang J, Huang T, Wang Y (2019) Fabrication of MCC/Cu_2O/Go composite foam with high photocatalytic degradation ability toward methylene blue. Carbohydr Polym 223:115101. https://doi.org/10.1016/j.carbpol.2019.115101
47. Wang L, Ji Z, Lin J, Li P (2017) Preparation and optical and photocatalytic properties of Ce-doped ZnO microstructures by simple solution method. Mater Sci Semicond Process 71:401–408. https://doi.org/10.1016/j.mssp.2017.09.001